

Supramolecular Helicates

Encapsulation Enhances the Quantum Coherence of a Solid-State Molecular Spin Qubit

Abinash Swain, Leoní A. Barrios, Yulia Nelyubina, Simon J. Teat, Olivier Roubeau, Valentin Novikov,* and Guillem Aromí*

Abstract: Spins within molecules benefit from the atomistic control of synthetic chemistry for the realization of qubits. One advantage is that the quantum superpositions of the spin states encoding the qubit can be coherently manipulated using electromagnetic radiation. The main challenge is the fragility of these superpositions when qubits are to partake of solid-state devices. We address this issue with a supramolecular approach for protecting molecular spin qubits against decoherence. The molecular qubit $[\text{Cr}(\text{ox})_3]^{3-}$ has been encapsulated inside the diamagnetic triple-stranded helicate $[\text{Zn}_2\text{L}_3]^{4+}$ (L is a *bis*-pyrazolylpyridine ligand). The quantum coherence of the protected qubit is then analyzed with pulsed EPR spectroscopy and compared with the unprotected qubit, both in solution and in the solid state. Crucially, the spin–spin relaxation in the solid state has been examined within diamagnetic crystal lattices of the isostructural $([\text{Al}(\text{ox})_3]@[\text{Zn}_2\text{L}_3])^+$ or $[\text{Al}(\text{ox})_3]^{3-}$ assemblies, respectively, doped with the Cr^{3+} qubit in two different (<10%) concentrations. The study unveils a surprising increase of the phase memory time of the qubit upon encapsulation only in the solid. Spin-lattice relaxation times also exhibit a significant enhancement, as established from inversion recovery pulse sequences and from slow relaxation of the magnetization of the protected qubit, not featured by the free qubit.

The ongoing second quantum revolution is set to drastically advance current technologies and profoundly reshape our way of life. This transformation is driven by the ability to harness quantum properties through increasingly precise control of matter at the nanoscale.^[1] One of the most anticipated breakthroughs is quantum computing (QC), which leverages

fundamental principles of quantum mechanics (such as superposition and entanglement) to process information via quantum algorithms.^[2] To realize this potential, quantum computing requires technologies that meet critical requirements, including scalability and quantum error correction. Achieving these capabilities necessitates wiring up a sufficiently large number of identical qubits, a challenge that continues to constrain even the most advanced implementations.^[3,4] A promising emerging alternative involves using electronic or nuclear spins within molecules to create qubits and quantum gates.^[5–8] This approach enables the development of multi-qubit architectures with atomic-level control over topology, interqubit interactions, and the surrounding environment, offering unmatched reproducibility. Molecular quantum processors capable of implementing quantum error correction with a small number of qubits have already been proposed.^[3,9] Additionally, chemical engineering has helped significantly to increase the quantum coherence of electronic spins of molecules.^[10–19] At this stage, the challenge is to preserve the quantum superpositions of qubits when they become part of hybrid solid-state devices for their implementation.^[20–22] One promising approach is their encapsulation into cages, protecting them from sources of decoherence while being transferred to the appropriate locations. Using fullerenes to host qubits is a promising strategy to achieve this goal but limits enormously the ability to chemically tune the nature and environment of the qubits.^[23–27]

We employ here a purely synthetic chemistry approach to protect spin qubits in the solid state by encapsulating them within a suited supramolecular host. As a qubit realization, we selected the Cr(III) center in the complex $[\text{Cr}(\text{ox})_3]^{3-}$ (ox = dianion of oxalic acid), which has been shown to


[*] A. Swain, L. A. Barrios, V. Novikov, G. Aromí
Departament de Química Inorgànica i Orgànica, Universitat de Barcelona, Diagonal 645, Barcelona 08028, Spain
E-mail: novikov@ub.edu
aromi@ub.edu


A. Swain, L. A. Barrios, V. Novikov, G. Aromí
Department Institute of Nanoscience and Nanotechnology of the University of Barcelona (IN2UB), University of Barcelona, Barcelona, Spain

Y. Nelyubina
Nesmeyanov Institute of Organoelement Compounds, Russian Academy of Sciences, Moscow 119334, Russia

S. J. Teat
Advanced Light Source, Berkeley Laboratory, 1 Cyclotron Road, Berkeley, CA 94720, USA

O. Roubeau
Instituto de Nanociencia y Materiales de Aragón (INMA), CSIC and Universidad de Zaragoza, Plaza San Francisco s/n, Zaragoza 50009, Spain

 Additional supporting information can be found online in the Supporting Information section

 © 2025 The Author(s). Angewandte Chemie International Edition published by Wiley-VCH GmbH. This is an open access article under the terms of the [Creative Commons Attribution](https://creativecommons.org/licenses/by/4.0/) License, which permits use, distribution and reproduction in any medium, provided the original work is properly cited.

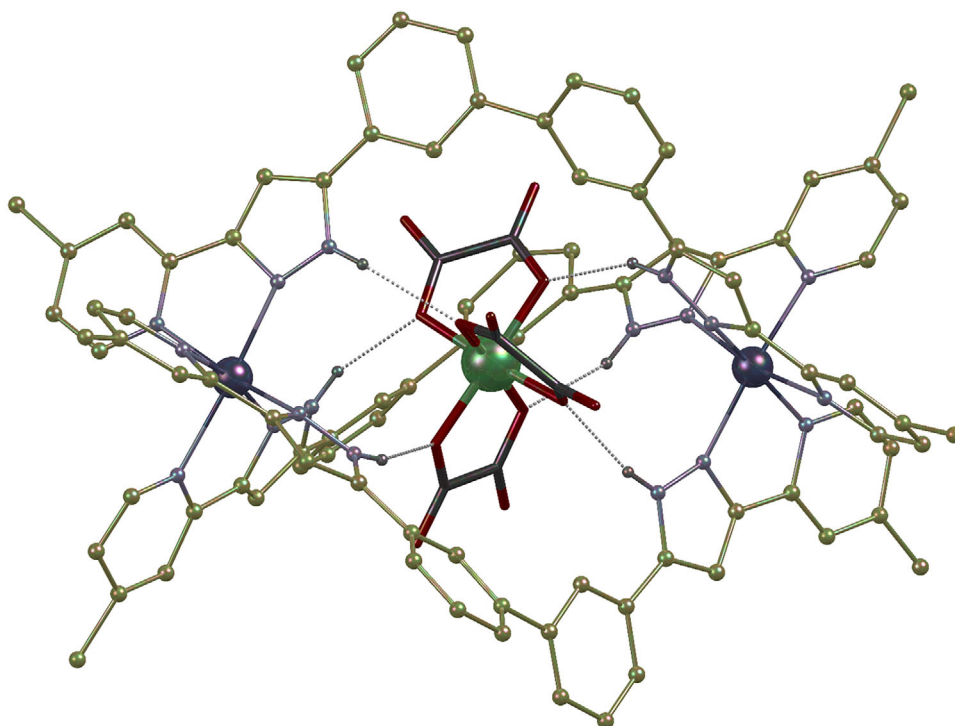


Figure 1. Molecular structure of the cationic assembly $([\text{Cr}(\text{ox})_3]@[\text{Zn}_2\text{L}_3])^+$ in **1**. The $[\text{Zn}_2\text{L}_3]^{4+}$ host is represented in ball-and-stick style (where C, yellow balls; Zn, large deep-purple balls; N, medium purple balls; and H, small purple balls). The encapsulated species is in a capped stick style except for the Cr atom (C, grey; O, red; and Cr, green). Hydrogen atoms but these from N–H groups are omitted. Hydrogen bonds are shown as black dotted lines.

coherently encode qubits through any of the transitions within its axially anisotropic $S = 3/2$ spin state.^[28,29] We show that this complex can be adequately positioned inside the cavity of a diamagnetic $[\text{Zn}_2\text{L}_3]^{4+}$ supramolecular triple-stranded helicate (L being a ligand formed by a biphenyl group separating two pyrazolypyridine coordination pockets). The protected qubit is obtained by reaction of $\text{K}_3[\text{Cr}(\text{ox})_3]$ with a solution of ZnCl_2 and L in the presence of 18-crown-6 as crystals of the ionic assembly $[\text{Cr}(\text{ox})_3]@[\text{Zn}_2\text{L}_3]\text{Cl}$ (**1**). Its single-crystal X-ray diffraction (SCXRD) analysis (Figures 1, S1, and S2) reveals that the octahedral qubit is suited to fit the cavity of the host with the assistance of six $[\text{O}\cdots\text{H}\cdots\text{N}]$ hydrogen bonds between the oxalate donor O-atoms and the H-atoms riding the pyrazolyl rings of the L ligands. The chirality of the ZnN_6 octahedral centers of the host is correlated with that of the central $[\text{Cr}(\text{ox})_3]^{3-}$ moiety, in turn defining the handedness of the helical architecture. Both enantiomers of the ensemble are present in the monoclinic lattice of **1** ($C2/c$ space group, see Tables S1–S3). This lattice contains four formula units of the compound, maintaining the Cr(III) ions separated 12.318 Å apart or more.

The full $([\text{Cr}(\text{ox})_3]@[\text{Zn}_2\text{L}_3])^+$ assembly was observed by MALDI-TOF mass spectrometry (MS) thus corroborating its integrity in $\text{H}_2\text{O}:\text{MeOH}$ solution (Figure S3), while the magnetic structure of the encapsulated $[\text{Cr}(\text{ox})_3]^{3-}$ qubit was confirmed by CW X-band EPR in DMF solution (Figure S4).

For the proposed modular approach to qubit protection, the quantum dynamic behavior in the solid state is particularly relevant. To investigate these properties, it was

essential to isolate the encapsulated qubits within a matrix that maintains a large separation between them. To do so, a diamagnetic analogue of the crystal lattice of **1** — the compound $[\text{Al}(\text{ox})_3]@[\text{Zn}_2\text{L}_3]\text{Cl}$ (**2**) — was synthesized using Al instead of Cr. It is isostructural with **1** (Figures S5 and S6, Tables S1–S3) and exhibits analogous MS properties (Figure S7). This structural correspondence suggests the possibility of doping the lattice of **2** with dispersed $([\text{Cr}(\text{ox})_3]@[\text{Zn}_2\text{L}_3])^+$ supramolecular cations to form a solid solution. This doping was successfully achieved at two different concentrations, resulting in lattices with ICP-determined molar Al:Cr ratios of 0.91:0.09 (**3**) and 0.97:0.03 (**4**), respectively, obtained using mixtures of $\text{K}_3[\text{M}(\text{ox})_3]$ ($\text{M} = \text{Al}$ and Cr) in the respective stoichiometric amounts. The SCXRD structure of **4** (Figure S8 and Tables S1–S3) is analogous to that of **1** and **2** and agrees with the ICP results (see Supporting Information). The MS of the microcrystalline molecular alloys unveils both versions of $([\text{M}(\text{ox})_3]@[\text{Zn}_2\text{L}_3])^+$ ($\text{M} = \text{Al}$ and Cr) in the appropriate proportions (Figures S9 and S10). The isostructural nature of **1**, **2**, **3**, and **4** in the bulk was confirmed by powder X-ray diffraction (PXRD) at room temperature (Figure S11) as well as IR spectroscopy (Figure S12).

The magnetic properties of the $[\text{Cr}(\text{ox})_3]^{3-}$ qubit in the lattices of **1**, **3**, and **4** were studied by magnetometry and X-band EPR spectroscopy. For all these measurements, the solids used did certainly not retain the same solvate molecules as those observed by SCXRD. The composition was expected to coincide with that determined by microanalysis (see Supporting Information), thus leading to a slightly modified

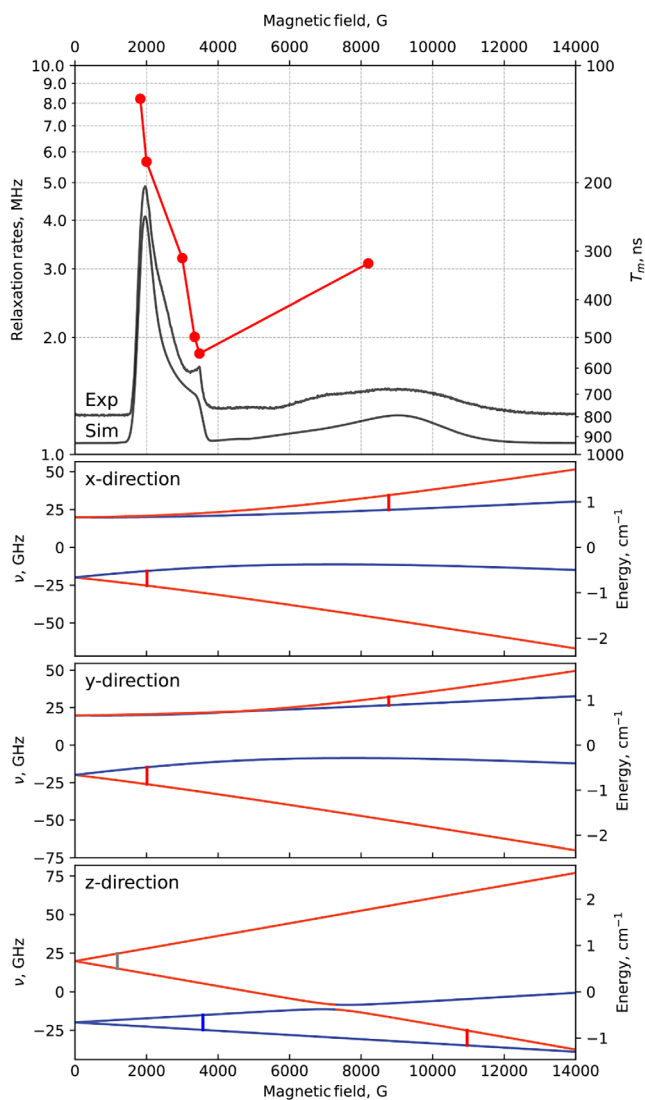


Figure 2. Top panel: Pulsed EPR data of a polycrystalline sample of **4**, without grinding, at 10 K (X-band): field-dependence of the phase memory time and corresponding relaxation rates (●, connecting lines are a guide to the eye), plotted on the same magnetic field axis as the experimental and simulated echo detected field sweep (EDFS) EPR spectra of **4**. Lower panels: Energy level diagrams for different orientations of the magnetic field, corresponding to the simulated spectrum with $g_x = 1.86(7)$, $g_y = 1.90(9)$, $g_z = 1.94(7)$, $D = 0.660(6)$ cm^{-1} , and $E = 0.030(0)$ cm^{-1} . The colors of the levels correspond to the predominant contribution of the $m_s = \pm 1/2$ (blue) or $m_s = \pm 3/2$ (red) states. Inter-Kramers transitions within the $m_s = \pm 1/2$ states are shown in blue, transitions between states with different $|m_s|$ values in red, forbidden transitions in gray.

crystal lattice. The CW EPR spectra exhibit the typical features of an $S = 3/2$ system with slight anisotropy, which is satisfactorily simulated with $g_x = 1.86(7)$, $g_y = 1.90(9)$, $g_z = 1.94(7)$, $D = 0.660(6)$ cm^{-1} , and $E = 0.030(0)$ cm^{-1} . No significant variations are observed among the spectra of undiluted and diluted solid-state samples or with liquid-phase DMF solution measurements (Figure 2, of **4**, where the complex acts as dopant in 3%; **S4**, of **1** dissolved in DMF; Figure S14, of solid **1**, with 100% of the guest being the Cr(III)

complex), thus confirming the persistence of the encapsulated qubit's magnetic parameters across different environments. The variable field and temperature magnetization data of **1** are consistent with a paramagnetic species with $S = 3/2$ and $g = 2.17$ and are reproduced using the same spin Hamiltonian parameters as for the CW EPR spectra (Figure S13). Compound **3** exhibits the same behavior if an Al:Cr ratio of 0.94:0.06 is considered, in reasonable agreement with ICP results (vide supra).

The dynamic magnetic properties were first investigated with frequency-dependent ac susceptibility on the concentrated solid compound **1**. At 2 K, the application of a dc field as low as 0.025 T induces the rise of an out-of-phase component of the magnetic susceptibility, χ'' , indicating slow relaxation of the magnetization (Figures S15–S17). This unique behavior for the Cr(III) ion was originally reported by us in the $[\text{Cr}(\text{ox})_3]^{3-}$ complex upon encapsulation by a ferrous $[\text{Fe}_2\text{L}_3]^{4+}$ cage.^[30] In **1**, a slower relaxation mode of the $([\text{Cr}(\text{ox})_3]@[\text{Zn}_2\text{L}_3])^+$ species emerges for applied dc fields above 0.2 T. The characteristic relaxation times, τ , for the main, faster mode reach up to 10 ms for $B = 2000$ G. Temperature-dependent measurements across a temperature range of 2–7 K were also performed at this applied dc field. The thermal dependence of τ follows a power-law with an exponent close to -2 ($\tau \propto T^{-1.94}$, Figure S17), consistent with a direct relaxation process dominated by a phonon bottleneck. The latter may be due to a relaxation pathway mediated exclusively by the molecular vibrations of the encapsulated qubit while isolated from those of the lattice, in sharp contrast to the absence of slow relaxation of the magnetization observed for $\text{K}_3[\text{Cr}(\text{ox})_3]$, even upon the application of an external dc field.^[30] We recently suggested the emergence of such sublattice of vibrations for the relaxation in $\text{guest}@[\text{Co}_2]$ helicates.^[31]

The spin-lattice relaxation times T_1 of $[\text{Cr}(\text{ox})_3]^{3-}$ in **3** and **4** were also determined using pulsed EPR at various temperatures (4–25 K) and $B = 3480$ G through inversion recovery experiments (Figures S18 and S19). The resulting T_1 values, determined by fitting the echo intensity curves to stretched exponential functions, are consistent with the relaxation times τ obtained from ac magnetic susceptibility studies on **1** (Figure 3a), further supporting the presence of a dominant phonon bottleneck. This coincidence is surprising considering that both methods of determination are very different, one based on a thermodynamic bulk measurement and the other being spectroscopic, in addition to the fact that the magnetic measurements are performed on a pure compound whereas the pulsed EPR determinations are performed on diluted samples.

The effect of the encapsulation on the solid-state quantum coherence of the $[\text{Cr}(\text{ox})_3]^{3-}$ qubit was then analyzed by pulsed EPR on **3** and **4**. In both cases, the EDFS spectra are identical to those observed in CW measurements both for the magnetically concentrated solid samples and DMF solutions (Figures S20 and S21) and are simulated using the same spin Hamiltonian parameters (see above). The phase memory time of **4** at different magnetic fields was evaluated by fitting the Hahn echo decay curves to stretched exponentials (Figure S22). As relaxation times are affected by the nature of the

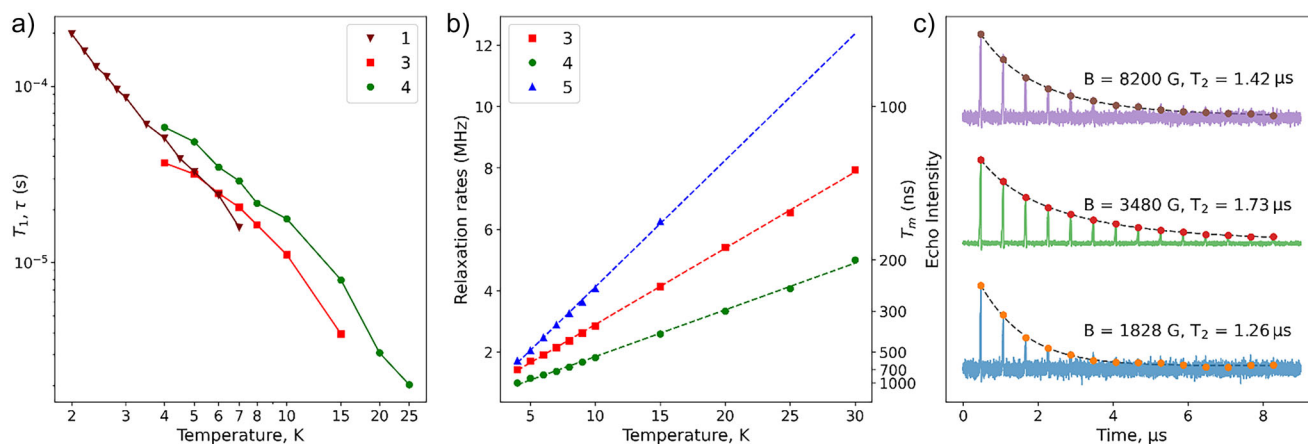


Figure 3. Relaxation data obtained by pulsed EPR and magnetic susceptibility measurements: a) Temperature-dependence of spin–lattice relaxation times for $[\text{Cr}(\text{ox})_3]@[\text{Zn}_2\text{L}_3]^+$ at different Cr(III) concentrations in the solid-state solutions. Plots are from Cr(III) contents of 100% (**1**, by *ac*-magnetometry), 9% and 3% (**3** and **4**, by EPR), lines are to guide the eye. b) Temperature-dependence of decoherence rates for **3**, **4**, and **5**; c) Results of CPMG for **4**, showing the transient responses at 1828, 3480, and 8200 G at 4 K, with amplitudes estimated by integrating each echo and fitting with a stretched exponential.

corresponding EPR transitions,^[29] we analyzed the Zeeman diagrams associated with them (Figure 2). The contributions of the different spin manifolds to EPR transitions have a clear impact on their associated T_m . The longest relaxation times (i.e., slowest relaxation rates) are observed at magnetic fields corresponding to transitions among the $m_s = \pm 1/2$ states along the *z*-axis. In contrast, inter-Kramers transitions result in significantly shorter T_m (Figure 2).

The temperature dependence of T_m in the solid state was investigated for the most coherent transition (at $B = 3480$ G). As expected, the magnetic relaxation in the sample with 3% of Cr is slower than in that with 9%, both showing strong temperature dependence (e.g., 1 μs versus 0.7 μs at 4 K; Figures S23 and S24). In all cases, T_m remains smaller than T_1 by more than one order of magnitude; therefore, the spin-lattice relaxation does not limit quantum coherence in these systems.

Note that the phase memory times at all temperatures were significantly longer than those of the free $[\text{Cr}(\text{ox})_3]^{3-}$ species, even when the latter was measured within the crystal lattice of $\text{K}_3[\text{Al}(\text{ox})_3]$ doped with $\sim 1\%$ of $[\text{Cr}(\text{ox})_3]^{3-}$ (**5**). Thus, T_m in **5** is shorter than in **3**, which contains 9% of paramagnetic ions, even though a simple model based on the average Cr–Cr distance (see Supporting Information: Discussion) predicted much stronger dipole–dipole interactions in **3**. Such behavior indicates that dipolar interactions are not the main cause of decoherence in this system. A more concentrated version of compound **5**, with 7% Cr (**6**), was also prepared (see Supporting Information) but is not discussed here.

Further insight into the mechanism of spin relaxation comes from a combined analysis of the field and temperature dependences of T_m . For samples **3–5**, the spin–spin relaxation rates ($1/T_m$) scale linearly with temperature (Figure 3b), strongly suggesting a phonon-driven decoherence.^[32] Although phonon-induced processes are typically associated with spin-lattice relaxation^[33] and affect

T_1 , they can also reduce T_m by modulating terms in the spin Hamiltonian, thereby shifting the resonance frequency and causing spectral diffusion and accelerated decoherence. The field-dependence of T_m , which shows faster decoherence at positions corresponding to inter-Kramers transitions, supports this interpretation (Figure 2). These transitions experience stronger spin–orbit coupling and are more sensitive to phonon-induced fluctuations of the zero-field splitting than transitions within the $m_s = \pm 1/2$ doublet, leading to shorter coherence times. Along these lines, applying a Carr–Purcell–Meiboom–Gill (CPMG) sequence^[34] to sample **4** increased the phase memory time and markedly reduced its field dependence (Figure 3c). The narrower T_m range under CPMG (1.26–1.70 μs) compared to its nearly five-fold variation with only Hahn echo sequences (Figure 2) suggests that phonon-driven spectral diffusion dominates decoherence in this regime.

From the above analysis, it follows that the increased coherence time in the solid state observed for $[\text{Cr}(\text{ox})_3]@[\text{Zn}_2\text{L}_3]^+$ following the encapsulation of the $[\text{Cr}(\text{ox})_3]^{3-}$ qubit into the cavity of the supramolecular helicate can be attributed to the reduced phonon contribution to decoherence. It likely arises from significant differences in the phonon environments of the two hosts. In the inorganic $\text{K}_3[\text{Al}(\text{ox})_3]$ lattice, strongly coupled phonon modes efficiently interact with the electronic states of Cr(III) ions. In contrast, encapsulating individual $[\text{Cr}(\text{ox})_3]^{3-}$ units in a relatively flexible metal–organic cavity leads to lower phonon density, weaker vibrational coupling to the metal center, and greater decoupling of the spin from the rigid lattice.

Further supporting this conclusion, dissolution of free $[\text{Cr}(\text{ox})_3]^{3-}$ leads to a significant increase in T_m (Figure S25), consistent with the disappearance of strong lattice phonons. On the contrary, dissolving $[\text{Cr}(\text{ox})_3]@[\text{Zn}_2\text{L}_3]^+$ does not improve its relaxation properties. Indeed, a standard Hahn echo pulse sequence of the latter species^[35] yields a phase

memory time of $T_m = 602$ ns at 4 K (Figure S26), similar to that derived in the solid state, while the EDFS spectrum (Figure S4) of the solution agrees with its CW counterpart. This indicates that the vibrations involved in the relaxation remain the same as in the solid state and are localized rather than extended, also in agreement with the proposed origin of phonon bottleneck affecting T_1 .

Taken together, these results confirm the validity of the encapsulation approach as a strategy for stabilizing quantum superpositions of qubits in the solid state by isolating them from lattice vibrations.

The spin dynamics of $[\text{Cr}(\text{ox})_3]^{3-}$ in sample **4** was further explored via nutation experiments at different magnetic fields. The echo decay as a function of nutation pulse length shows Rabi oscillations (Figures S27–S29), with frequencies, Ω_R , proportional to microwave field B_1 , confirming the possibility to reliably manipulate the qubit and put it into arbitrary superposition states for all the tested fields. The best qubit figure of merit extracted from these experiments is $T_m/T_G = 216$, where T_G is the gate time defined as the duration of a π -pulse (8 ns) at the highest applied microwave power of 3.5 dB at magnetic field of 3480 G.

In conclusion, we have demonstrated that encapsulating the molecular spin-qubit $[\text{Cr}(\text{ox})_3]^{3-}$ within the diamagnetic triple-stranded helicate $[\text{Zn}_2\text{L}_3]^{4+}$ significantly improves its quantum coherence in the solid state. Through extensive use of pulsed EPR spectroscopy, we observed a notable increase in phase memory time and spin-lattice relaxation time compared to the unprotected qubit. The encapsulation mitigates decoherence mainly by reducing phonon coupling to the chromium ion; the softer, vibrationally decoupled environment of the supramolecular host lowers the impact of spectral diffusion and extends the phase memory time. More broadly, our findings challenge the prevailing trade-off between chemical functionality and quantum performance: while synthetic modifications often introduce magnetic noise and compromise coherence, we demonstrate that embedding the qubit within a large supramolecular host can instead enhance it. This opens the door to incorporating switchable units, tunable spin–spin couplings, or surface anchoring groups without sacrificing coherence—a critical step toward functional quantum molecular devices.

Supporting Information

Synthesis procedure, spectroscopic data,^[36] and crystallographic details. This material is available free of charge via the Internet at <http://XX>. The authors have cited additional references within the Supporting Information.^[37–48]

Acknowledgements

This research was supported by the Spanish Ministry of Science (TED2021-129214B-I00, PID2022-137764OB-I00, PID2020-118329RB-I00, PID2023-150767OB-I00, BG22/00039, and PRTR-C17.I1), the Aragón Government (E31_23R PLATON), and Advanced Light Source, which

is a DOE Office of Science User Facility under contract no. DEAC02-05CH11231. VN thanks the Spanish Ministry of Science for a “Beatriz Galindo” grant (BG22/00039). GA thanks the Generalitat de Catalunya for Next Generation cofund (PRTR-C17.I1) and the prize ICREA Academia 2023. The authors thank the Biomolecular Mass Spectrometry Analysis Unit from Scientific and Technological Centers (CCiTUB), Universitat de Barcelona, and Irene Fernández Vidal and Laura Ortiz Vera for their support and advice on MALDI-TOF measurements.

Conflict of Interests

The authors declare no conflict of interest.

Data Availability Statement

The data that support the findings of this study are available from the corresponding author upon reasonable request.

Keywords: Molecular spin-qubit • Quantum coherence • Rabi oscillations • Supramolecular helicates • Time-resolved EPR

- [1] J. P. Dowling, G. J. Milburn, *Philos. Transact. A Math. Phys. Eng. Sci.* **2003**, *361*, 1655–1674.
- [2] M. A. Nielsen, I. L. Chuang, *Quantum Computation and Quantum Information: 10th Anniversary Edition*, Cambridge University Press, Cambridge **2010**.
- [3] E. Macaluso, M. Rubín, D. Aguilà, A. Chiesa, L. A. Barrios, J. I. Martínez, P. J. Alonso, O. Roubeau, F. Luis, G. Aromí, S. Carretta, *Chem. Sci.* **2020**, *11*, 10337–10343.
- [4] T. Monz, D. Nigg, E. A. Martinez, M. F. Brandl, P. Schindler, R. Rines, S. X. Wang, I. L. Chuang, R. Blatt, *Science* **2016**, *351*, 1068–1070.
- [5] A. Chiesa, P. Santini, E. Garlatti, F. Luis, S. Carretta, *Rep. Prog. Phys.* **2024**, *87*, 034501.
- [6] A. Gaita-Ariño, F. Luis, S. Hill, E. Coronado, *Nat. Chem.* **2019**, *11*, 301–309.
- [7] M. Atzori, R. Sessoli, *J. Am. Chem. Soc.* **2019**, *141*, 11339–11352.
- [8] G. Aromí, D. Aguilà, P. Gamez, F. Luis, O. Roubeau, *Chem. Soc. Rev.* **2012**, *41*, 537–546.
- [9] R. Hussain, G. Allodi, A. Chiesa, E. Garlatti, D. Mitcov, A. Konstantatos, K. S. Pedersen, R. De Renzi, S. Piligkos, S. Carretta, *J. Am. Chem. Soc.* **2018**, *140*, 9814–9818.
- [10] D. Kaminski, A. L. Webber, C. J. Wedge, J. J. Liu, G. A. Timco, I. J. Vitorica-Yrezabal, E. J. L. McInnes, R. E. P. Winpenny, A. Ardavan, *Phys. Rev. B* **2014**, *90*, 184419.
- [11] Y.-S. Zhang, Y.-F. Fan, X.-Q. Tao, G.-Y. Li, Q.-S. Deng, Z. Liu, Y.-X. Wang, S. Gao, S.-D. Jiang, *J. Mater. Chem. C* **2024**, *12*, 5150–5156.
- [12] N. P. Kazmierczak, R. Mirzoyan, R. G. Hadt, *J. Am. Chem. Soc.* **2021**, *143*, 17305–17315.
- [13] M. Shiddiq, D. Komijani, Y. Duan, A. Gaita-Ariño, E. Coronado, S. Hill, *Nature* **2016**, *531*, 348–351.
- [14] L. C. de Camargo, M. Brigantí, F. S. Santana, D. Stinghen, R. R. Ribeiro, G. G. Nunes, J. F. Soares, E. Salvadori, M. Chiesa, S. Benci, R. Torre, L. Sorace, F. Totti, R. Sessoli, *Angew. Chem. Int. Ed.* **2021**, *60*, 2588–2593.

- [15] K. Bader, D. Dengler, S. Lenz, B. Endeward, S.-D. Jiang, P. Neugebauer, J. Van Slageren, *Nat. Commun.* **2014**, *5*, 5304.
- [16] M. Rubín-Osanz, F. Lambert, F. Shao, E. Rivière, R. Guillot, N. Suaud, N. Guihéry, D. Zueco, A.-L. Barra, T. Mallah, F. Luis, *Chem. Sci.* **2021**, *12*, 5123–5133.
- [17] C. J. Yu, M. J. Graham, J. M. Zadrozny, J. Niklas, M. D. Krzyaniak, M. R. Wasielewski, O. G. Poluektov, D. E. Freedman, *J. Am. Chem. Soc.* **2016**, *138*, 14678–14685.
- [18] C.-Y. Lin, T. Ngendahimana, G. R. Eaton, S. S. Eaton, J. M. Zadrozny, *Chem. Sci.* **2019**, *10*, 548–555.
- [19] R. Stewart, A. B. Canaj, S. L. Liu, E. R. Martí, A. Celmina, G. Nichol, H. P. Cheng, M. Murrie, S. Hill, *J. Am. Chem. Soc.* **2024**, *146*, 11083–11094.
- [20] M. D. Jenkins, D. Zueco, O. Roubeau, G. Aromí, J. Majer, F. Luis, *Dalton Trans.* **2016**, *45*, 16682–16693.
- [21] I. Gimeno, A. Urtizberea, J. Román-Roche, D. Zueco, A. Camón, P. J. Alonso, O. Roubeau, F. Luis, *Chem. Sci.* **2021**, *12*, 5621–5630.
- [22] A. Repollés, M. C. Pallarés, D. Aguilà, O. Roubeau, V. Velasco, D. Gella, L. A. Barrios, M. J. Martínez-Pérez, J. Sesé, D. Drung, J. I. Martínez, T. Schurig, B. Le Guennic, A. Lostao, G. Aromí, F. Luis, *Nanoscale* **2025**, *17*, 219–229.
- [23] Z. Hu, B.-W. Dong, Z. Liu, J.-J. Liu, J. Su, C. Yu, J. Xiong, D.-E. Shi, Y. Wang, B.-W. Wang, A. Ardavan, Z. Shi, S.-D. Jiang, S. Gao, *J. Am. Chem. Soc.* **2018**, *140*, 1123–1130.
- [24] R. M. Brown, A. M. Tyryshkin, K. Porfyrakis, E. M. Gauger, B. W. Lovett, A. Ardavan, S. A. Lyon, G. A. D. Briggs, J. J. L. Morton, *Phys. Rev. Lett.* **2011**, *106*, 110504.
- [25] Z. Liu, B. W. Dong, H. B. Meng, M. X. Xu, T. S. Wang, B. W. Wang, C. R. Wang, S. D. Jiang, S. Gao, *Chem. Sci.* **2018**, *9*, 457–462.
- [26] J. Qiu, L. Abella, X. Du, Z. Cao, Z. He, Q. Meng, Y. Yan, J. M. Poblet, L. Sun, A. Rodríguez-Fortea, N. Chen, *J. Am. Chem. Soc.* **2024**, *146*, 24310–24319.
- [27] P. X. Fu, S. Zhou, Z. Liu, C. H. Wu, Y. H. Fang, Z. R. Wu, X. Q. Tao, J. Y. Yuan, Y. X. Wang, S. Gao, S. D. Jiang, *Angew. Chem. Int. Ed.* **2022**, *61*, e202212939.
- [28] M. J. Graham, J. M. Zadrozny, M. Shiddiq, J. S. Anderson, M. S. Fataftah, S. Hill, D. E. Freedman, *J. Am. Chem. Soc.* **2014**, *136*, 7623–7626.
- [29] M. S. Fataftah, J. M. Zadrozny, S. C. Coste, M. J. Graham, D. M. Rogers, D. E. Freedman, *J. Am. Chem. Soc.* **2016**, *138*, 1344–1348.
- [30] M. Darawsheh, L. A. Barrios, O. Roubeau, S. J. Teat, G. Aromí, *Angew. Chem. Int. Ed.* **2018**, *57*, 13509–13513.
- [31] L. A. Barrios Moreno, N. Capó, H. Boulehour, D. Reta, I. Tejedor, O. Roubeau, G. Aromí, *Dalton Trans.* **2024**, *53*, 7611–7618.
- [32] J. Dolinšek, P. M. Cereghetti, R. Kind, *J. Magn. Reson.* **2000**, *146*, 335–344.
- [33] A. Abragam, B. Bleaney, *Electron Paramagnetic Resonance of Transition Ions*, OUP, Oxford **2012**.
- [34] S. Meiboom, D. Gill, *Rev. Sci. Instrum.* **1958**, *29*, 688–691.
- [35] E. Moreno-Pineda, D. O. T. A. Martins, F. Tuna, in *Electron Paramagnetic Resonance, Vol. 27*, The Royal Society of Chemistry **2021**, pp. 146–187.
- [36] Deposition numbers, 2416208 (for **1**), 2416209 (for **2**), and 2416210 (for **4**) contain the supplementary crystallographic data for this paper. These data are provided free of charge by the joint Cambridge Crystallographic Data Centre and Fachinformationszentrum Karlsruhe Access Structures service.
- [37] G. Pass, H. Sutcliffe, *Practical Inorganic Chemistry: Preparations, Reactions and Instrumental Methods*, Chapman and Hall, University of Michigan, Ann Arbor (USA) **1974**.
- [38] N. Capó, L. A. Barrios, J. Cardona, J. Ribas-Ariño, S. J. Teat, O. Roubeau, G. Aromí, *Chem. Commun.* **2022**, *58*, 10969–10972.
- [39] S. Stoll, A. Schweiger, *J. Magn. Reson.* **2006**, *178*, 42–55.
- [40] W. Kabsch, *Acta Crystallogr. D Biol. Crystallogr.* **2010**, *66*, 125–132.
- [41] C. Vonrhein, C. Flensburg, P. Keller, A. Sharff, O. Smart, W. Paciorek, T. Womack, G. Bricogne, *Acta Crystallogr. D Biol. Crystallogr.* **2011**, *67*, 293–302.
- [42] G. M. Sheldrick, Author, SAINT and SADABS, Bruker AXS Inc., Madison, Wisconsin, USA, **2012**.
- [43] G. M. Sheldrick, Author, CELL_NOW and TWINABS, Bruker AXS Inc., Madison, Wisconsin, USA, **2012**.
- [44] J. Juanhuix, F. Gil-Ortiz, G. Cuní, C. Colldelram, J. Nicolás, J. Lidón, E. Boter, C. Ruget, S. Ferrer, J. Benach, *J. Synchrotron Radiat.* **2014**, *21*, 679–689.
- [45] L. Krause, R. Herbst-Irmer, G. M. Sheldrick, D. Stalke, *J. Appl. Crystallogr.* **2015**, *48*, 3–10.
- [46] G. Sheldrick, *Acta Cryst. C* **2015**, *71*, 3–8.
- [47] G. Sheldrick, *Acta Cryst. A* **2015**, *71*, 3–8.
- [48] A. Spek, *Acta Cryst. C* **2015**, *71*, 9–18.

Manuscript received: May 14, 2025

Revised manuscript received: August 13, 2025

Accepted manuscript online: August 25, 2025

Version of record online: ■■■■■